

Kepler Bonus: Aperture Photometry Light Curves of EXBA Sources

JORGE MARTÍNEZ-PALOMERA ^{1,2}, CHRISTINA HEDGES ^{1,2}, JOSEPH E. RODRIGUEZ ³, GEERT BARENTSEN ^{1,2} AND
JESSIE DOTSON ²

¹Bay Area Environmental Research Institute, P.O. Box 25, Moffett Field, CA 94035, USA.

²NASA Ames Research Center, Moffett Field, CA, USA

³Department of Physics and Astronomy, Michigan State University, East Lansing, MI 48824, USA

ABSTRACT

NASA’s *Kepler* mission observed background regions across its field of view for more than three consecutive years using custom designed super apertures (EXBA masks). Since these apertures were designed to capture a region of the sky rather than single targets, the Kepler Science Data Processing pipeline produced Target Pixel Files, but did not produce light curves for the sources within these background regions. In this work we produce light curves for 9,327 sources observed in the EXBA masks. These light curves are generated using aperture photometry estimated from the instrument’s Pixel Response Function (PRF) profile computed from *Kepler*’s full-frame images. The PRF models enable the creation of apertures that follow the characteristic shapes of the PSF in the image and the computation of flux completeness and contamination metrics. The light curves are available at MAST as a High Level Science Product (`kbonus-apexba`). Alongside this dataset, we present `kepler-apertures`, a Python library to compute PRF models and use them to perform aperture photometry on *Kepler*-like data. Using light curves from the EXBA masks we found an exoplanet candidate around *Gaia* EDR3 2077240046296834304 consistent with a large planet companion with a $0.81R_J$ radius. Additionally, we report a catalog of 69 eclipsing binaries. We encourage the community to exploit this new dataset to perform in depth time domain analysis, such as eclipsing binaries demographic and others.

Keywords: Time Domain Astronomy – Light Curves – Exoplanets – Eclipsing Binaries – Astronomy databases

1. INTRODUCTION

NASA’s *Kepler* mission delivered to the community one of the finest time series datasets ever produced. *Kepler* observed more than 400,000 target stars (Borucki et al. 2010) *Kepler* found more than 4,000 exoplanet candidates (Thompson et al. 2018), observed numerous supernovae from earliest stages of explosion (Olling et al. 2015; Garnavich et al. 2016; Li et al. 2019), and more than 2,900 eclipsing binary systems (Kirk et al. 2016), to name some examples. The *Kepler* mission mainly downlinked image data around selected targets (KIC, Brown et al. 2011). These target cutouts are centered on the object of interest and usually cover a few pixels around the source. *Kepler* observations are organized

into seventeen 93-days periods. These observation periods are named quarters. The Kepler Science Data Processing Pipeline (Jenkins et al. 2010), produced two science products. First, the *Kepler* pipeline produced Target Pixel Files (TPFs), which are cutout images of each observed target. A TPF contains all observed cadences for the target in a single quarter as well as information on which pixels fall into the aperture of each target star. Secondly, the Light Curve Files (LCFs), which are flux time series of the target of interest. The LCFs contain two types of light curves, one is Simple Aperture Photometry (SAP), where the flux is measured within an aperture selected to minimize contamination from background sources. The second type are Presearch Data Conditioned Simple Aperture Photometry (PDCSAP) light curves (Smith et al. 2012) that corrects the SAP light curves for systematics of the instrument.

Kepler’s mission also downlinked single cadence observations of the entire *Kepler* field each month. These

Full Frame Images (FFIs) contain more than 1 million sources per image. They were observed mainly for calibration and diagnostic purposes (Van Cleve & Caldwell 2016). Although the FFIs covered the entire focal plane of the instrument, the time resolution is not comparable to the main targets observed with a cadence of 1 or 30 minutes. Montet et al. (2017) used *Kepler*'s FFIs to study long-term variability of Sun-like stars due to magnetic cycles. Additionally, two types of custom aperture targets were observed using the 30 min cadence mode. First, aperture masks covering two open clusters, NGC 6819 (Stello et al. 2010; Balona et al. 2013; Brewer et al. 2013) and NGC 6791 (Stello et al. 2011; Corsaro et al. 2012; McClure et al. 2021). The second custom masks are the background super apertures, or EXBA masks. The EXBA masks cover relatively dark regions of the sky at a common location on all CCD channels, and were observed continuously between quarters 5 and 17. The scientific motivation to collect these images was to obtain an unbiased characterization of the background Eclipsing Binary (EB) rate in the *Kepler* field (Barentsen et al. 2018).

The *Kepler* pipeline relied upon aperture photometry to create the flux time series of the targets. There are multiple ways to define the shape and the size of a photometric aperture. The simplest approach is defining circular apertures that enclose the source flux. A circular aperture would work well for isolated sources and where the instrument's Pixel Response Function (PRF) profile is symmetric (typically found in *Kepler* at the center of the focal plane). But a circular aperture will lose considerable flux where the PRF shape becomes distorted (typically when moving away from the center of the image) Aperture photometry can be improved by allowing for elliptical or non-circular shapes, e.g. isophote apertures. Regardless of shape simple apertures become sub-optimal in crowded regions, where source contamination is the dominant factor. Bryson et al. (2010) shows that *Kepler*'s PRF profiles are distorted at the edges of the focal plane, with elongated shapes in multiple directions. Therefore, the simple aperture methods will perform poorly. The *Kepler* pipeline performed photometry by computing optimized apertures for every target source and providing metrics that characterize the completeness of the flux, and amount of contamination within the aperture.

The EXBA masks were chosen to have an unbiased representation of the *Kepler* field. The number of Gaia sources (brighter than 20th magnitude in the *G* band) per channel mask fluctuates from less populated regions with a few dozens of objects to more crowded ones with a couple of hundred stars. In this work, we implement

aperture photometry by creating custom apertures that follow the PRF profile of the image. This PRF models are computed using *Kepler*'s FFIs and evaluated on every EXBA source. Until now, the EXBA masks have not been systematically analyzed and the *Kepler* pipeline did not produce LCFs for observed sources. In this work, we produce light curves for more than 9,300 sources detected in the EXBA masks. We follow the procedures introduced by the Linearized Field Deblending (LFD) photometry method (Hedges et al. 2021a) to obtain a detailed, yet fast to compute and evaluate, model of the PRF profile for all the channels in the focal plane of *Kepler*. Evaluating the PRF models on the EXBA sources provide a model of the object, which is used to define the photometric aperture and compute flux metrics. All the light curves produced in this work are publicly available to the community as FITS Light Curve Files and can be accessed throughout the Mikulski Archive for Space Telescopes (MAST) archive¹. We present `kepler-apertures`² (Martínez-Palomera 2021) a the set of Python tools to compute and use PRF models to perform aperture photometry on *Kepler*-like data. As an example of the opportunities that this new light-curve dataset provides, we perform a search of exoplanet transiting signals using the BLS periodogram method. We identify a candidate around the source *Gaia* EDR3 2077240046296834304 that shows a transiting signal consistent with a large planet or sub-stellar companion. Our search also provide a catalog of 69 EBs observed in the EXBA masks.

This article is structured as follows. Section 3 details the characteristics of the data used for this work as well as the steps followed to compute the PRF models, aperture photometry, flux metrics, and light curves. In Section 4 we present our results: high-level science products consisting of light curve files, and the search for transiting signals which resulted in an exoplanet candidate and a catalog of EBs. In Section 5 we discuss the opportunities that this new unexplored dataset provides to the community, as well as its limitations. Finally, Section 6 summarizes this work.

2. KEPLER OBSERVATIONS

The *Kepler* mission observed a specific area of the sky centered at R.A.= 19^h22^m40^s and Dec= +44°30'00" (J2000) between 2009 and 2013. The observations were split into quarters and taken in two cadence

¹ Kepler Bonus, APEXBA, <https://doi.org/10.17909/t9-d5wy-e535>

² <https://github.com/jorgemarpa/kepler-apertures/releases/tag/v0.1.0>

mode, a short 1-minute cadence and a long 30-minute cadence. The telescope camera is an array of 21 modules with two CCDs each. A CCD has two read-out channels adding to a total of 84 CCD channels. *Kepler* telescope has an aperture of 0.95 meters, a 105 square deg field-of-view, and the instrument has a pixel scale of 3.98 arcsec per pixel.

Typically three FFIs were downlinked during quarter 5 and 17, one at the beginning, middle, and end of the quarter. A single FFI channel has 1100×1024 pixels, adding to a total of 95 mega pixels for the entire focal plane. Each FFI has an exposure time of 27 minutes. *Kepler*'s FFIs can be downloaded from the MAST archive³.

The EXBA images were observed continuously between quarters 5 and 17 of *Kepler*'s prime mission using the long cadence setup. These data consist in 4 custom mask of 9×60 pixels per channel, each of these 4 tiles are located next to each other in the CCD producing a 36×60 pixel image per channel. *Kepler* EXBA images can be downloaded from the MAST archive⁴, by searching with the EXBA keyword in the *Investigation ID* field. An example of the tiled EXBA mask for channel 48 is shown in Figure 1. Valid data exist for 80 out of 84 channels. The four channels are missing because of failure of circuitry powering in module 3 of the camera (Van Cleve et al. 2016).

3. DATA PROCESSING

To obtain light curves based on aperture photometry that meet similar standards as those provided by *Kepler*'s pipeline in the main target LCFs, we follow these steps:

1. Create a detailed model of the PRF profile for each channel and quarter combination using *Kepler*'s FFIs.
2. Use Gaia catalogs to obtain accurate positions of the sources observed in the EXBA mask with a limiting magnitude of $G = 20$.
3. Obtain a flux-normalized model of each source by evaluating the PRF model on all Gaia sources observed in the EXBA mask.
4. Define multiple aperture masks according to the flux normalized source models and compute flux metrics that characterize them.

³ <https://archive.stsci.edu/missions-and-data/kepler/kepler-bulk-downloads>

⁴ <https://archive.stsci.edu/kepler/>

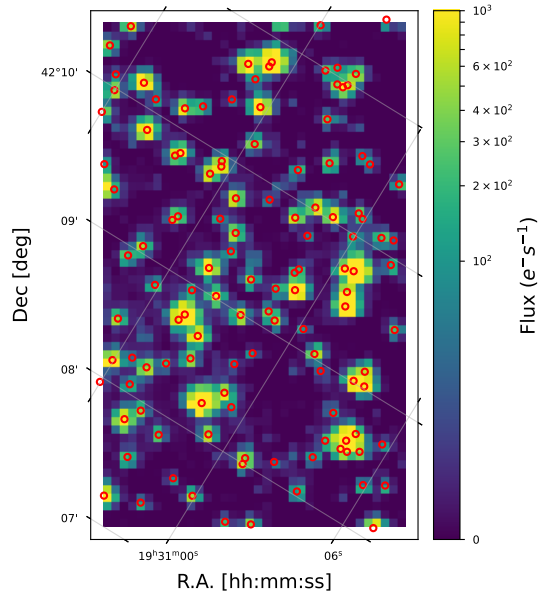


Figure 1. Example full EXBA mask (four tiles) for channel 48 observed during quarter 5. The image shown here is 36×60 pixels and the flux values averaged across cadences. 123 sources obtained from the Gaia EDR3 catalog down to $G \leq 20$ magnitude are marked with red circles (see Section 3.2). The brightest visible star is $G = 13.7$ magnitudes. Our pipeline filters out all contaminating sources within $2''$ to fit the PRF models. Sources outside the coverage of the mask (up to $4''$) are allowed and extracted for photometry.

5. Finally, compute multi-aperture photometry for every source, then compile and save the flux time series in FITS files following a similar structure as the LCFs.

The following sections describe these steps in detail.

3.1. Modeling the PRF Profile

Kepler's FFIs contain more than 1.1 million sources in total, on average $\sim 12,000$ sources can be detected in each channel. The large amount of sources available enables the creation of detailed PRF models for every channel.

To compute PRF models of each channel, we use the PRF scene modeling described in the LFD photometry method (Hedges et al. 2021a). This LFD photometry method uses Gaia catalogs to find and fix the coordinate position of sources in the image and models the scene PRF profile by fitting a linear model with spline basis to the data in polar coordinates. The PRF modeling done by the LFD method assumes the following: it relies upon the accurate astrometry done by Gaia catalogs; the PRF shapes do not vary significantly over the spatial scale of the detector channel; and the PRF shapes do not change in time within each quarter.

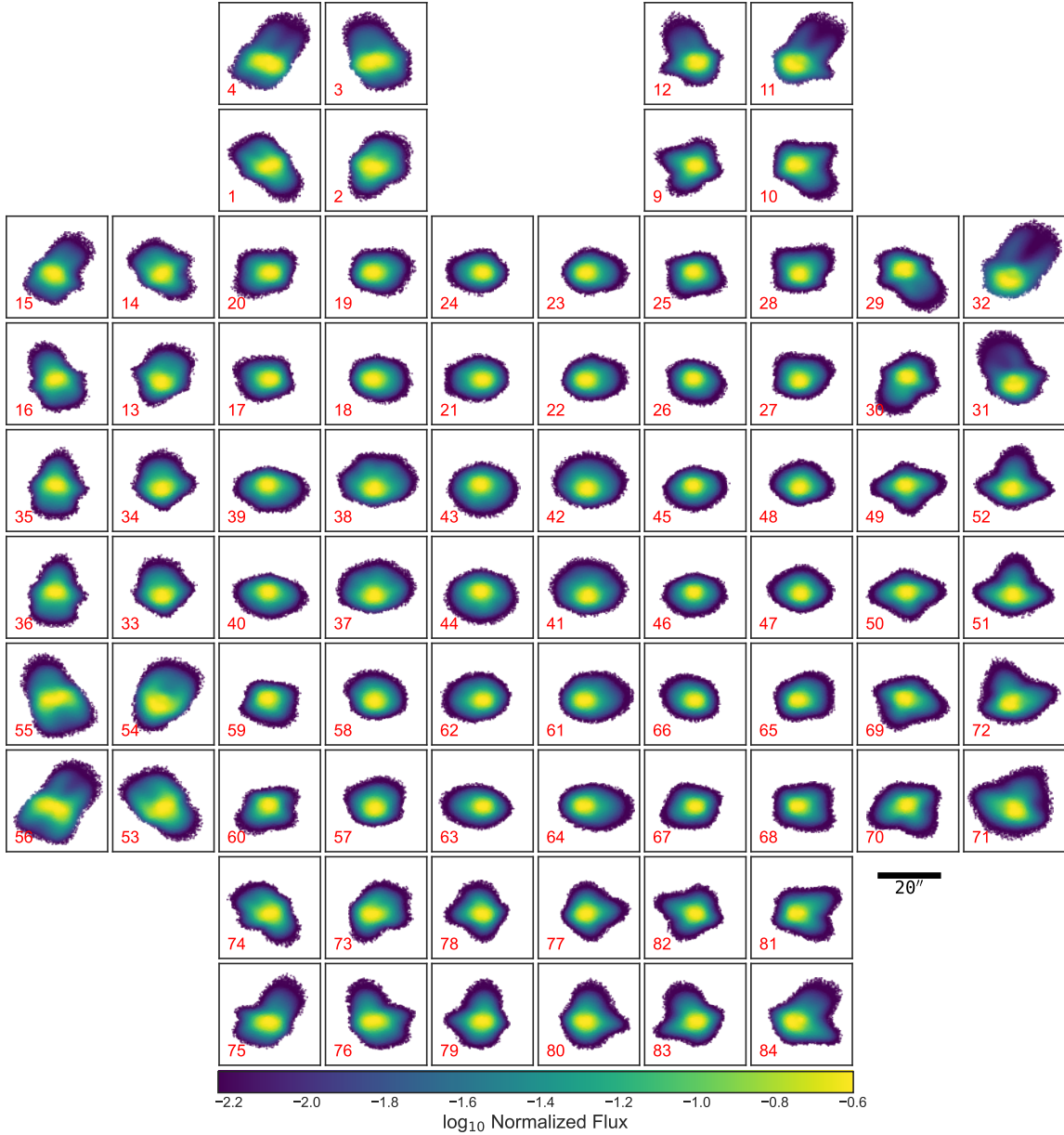


Figure 2. PRF models across the focal plane computed from *Kepler*'s FFIs as described in 3.1. The models are based on data observed during quarter 5. Each cell in the figure grid represents a single CCD channel (number in red). In a cell, each data point represents the pixel position from the reference source in Cartesian coordinates, while the color represents the pixel flux value normalized by the total flux of the corresponding reference source. As discussed in Hedges et al. (2021a), the PRF profiles show steep gradients and are elongated, particularly as we move away from the center of the focal plane. Note that in this figure the CCD channels have the axis origin at each cell's lower-left corner, then the orientations of the plotted PRFs do not reflect the axis origin of the CCD channels on *Kepler*'s focal plane which are arranged to be invariant under rotation. This is only aesthetics and does not affect the use of our models.

Figure 2 shows the PRF models for all 80 channels with available FFI data during quarter 5. At the center of the focal plane, the PRF shape is fairly circular, smooth, and shows angular symmetry. As we move away from the center, the PRF profile starts gradually showing elongation in both radial and tangential axis, this effect becomes extreme in the channels at the bor-

der. These characteristics of the data are conveniently captured by the model thanks to the use of polar coordinates, where the radial symmetry benefits the fit of a smoother model.

In Hedges et al. (2021a), the PRF profile is modeled using ~ 500 Gaia sources and around 7,000 pixel data points. The LFD method only uses pixel where flux

from the sources is detected and removes all background pixels. Here, in contrast, thanks to the large number of sources ($\sim 12,000$) in each FFI channel image, the number of pixels reach a larger value $\sim 100,000$, allowing for more dense and robust representation of the PRF. Additionally, [Hedges et al. \(2021a\)](#) models the drift in position of all sources due to velocity aberration, this correction is only necessary when doing LFD photometry on all cadences of a TPF stack to obtain light curves. In this work, we only follow the LFD method to obtain the PRF models from the FFIs and fitting the scene motion it is not only limited by the low number of FFI cadences but also out of the scope of this use-case. Computing the PRF models from *Kepler* FFIs can be computationally expensive, fortunately, the convenience use of `scipy`'s sparse matrices ([Virtanen et al. 2020](#)), keeps the memory use low ($\sim 450MB$ for a single PRF model) and computing time in the order of 100 seconds when using a modern personal laptop⁵. Evaluation of a PRF model is faster, for the same machine it takes ~ 1 milliseconds per source.

Our pipeline produce a total of 1,080 PRF models, one for every channel and quarter combination where the EXBA masks were collected. These PRF models can be later evaluated for a grid of positions (in Cartesian coordinates) to obtain a flux normalized model for either a single source or a set of sources in any *Kepler*-like data, e.g. TPFs, FFI, and SuperStamps⁶ files. Modeling the PRFs for every quarter capture the natural time degradation in sensitivity of the CCDs. The later is a factor that could have not been taken into account in [Bryson et al. \(2010\)](#) works due to the data availability, at the time of their work, only commissioning data was available. Furthermore, our PRF models use a small number of linear components which can be evaluated faster than grid-based models and are forced to be smooth with no edge effects. We direct the reader to [Hedges et al. \(2021a\)](#) for further discussion.

3.2. The EXBA Sources

We use Gaia EDR3 ([Gaia Collaboration et al. 2021](#)) as source catalog. This catalog provides high precision astrometry and source completeness, 0.5 mas at $G = 20$ and, complete between $G = 12$ and $G = 17$, respectively ([Fabricius et al. 2021](#)). Although Gaia G band ([Jordi et al. 2010](#)) does not exactly matches *Kepler*'s response

curve ([Van Cleve & Caldwell 2016](#)), it present an appropriate proxy for *Kepler* magnitudes and can be used as a observed source catalog. We query the Gaia catalog with a limiting magnitude of $G = 20$ and account for the source proper motions between each *Kepler*'s quarter and the Gaia EDR3 epoch. We flag contaminated sources ($< 5\%$) in crowded regions where the separation between sources is $< 2''$ (0.5 of a pixel), and we allow for sources outside the limits of the EXBA mask up to $4''$ (1 pixel). Only non-flagged sources will be extracted, but contaminants are considered when computing flux metrics (see following section for details). After this, a total of 9,327 (non-flagged) sources are found in the sky area covered by the EXBA mask (~ 0.2 sq. deg.) across all quarters. A CCD channel covers the same sky area every four quarters due to the rotation of the spacecraft between quarters. This effect, combined with the mask alignment in the rotational symmetric channels, leads to sources near the borders of the mask (within $20''$) to fall outside of it in certain quarters. As a result, 45% of the sources have observations in all 13 quarters while 13% of the sources have data in either 6, 7, or 11 quarters (see [Figure 3](#) for details).

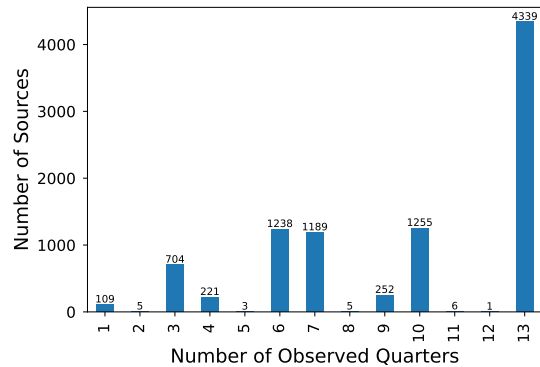


Figure 3. The number of EXBA sources with the total number of observed quarters. 46.5% of the total sources have observations in all 13 quarters that *Kepler* used the EXBA masks. The rest have 12 or fewer quarters available.

[Figure 4](#) shows the Color Magnitude Diagram (CMD) for both, main *Kepler* Targets and the EXBA sources. The object photometry comes from Gaia EDR3 catalog and their distances computed by [Bailer-Jones et al. \(2021\)](#). The EXBA sources follow the distribution of *Kepler*'s main targets except for the horizontal and asymptotic branches. A large fraction of the EXBA sources are located in the main sequence and binary sequence regions while a small fraction are evolved stars. The EXBA masks were chosen to be representative of the background field in comparison with the selection bias of

⁵ 2020 MacbookPro, 16 GB RAM, 2 GHz Quad-Core Intel Core i5 processor.

⁶ [Cody et al. \(2018\)](#) created SuperStamp FITS files for K2 observation of open clusters (M35, M67, Ruprecht 147, and NGC 6530) and the Galactic bulge.

Kepler's mission that specifically targeted evolved stars (Batalha et al. 2010).

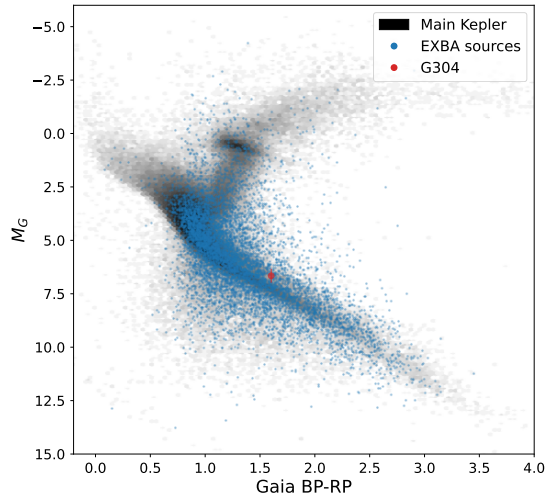


Figure 4. Color Magnitude Diagram of the EXBA sources (9,327 sources in blue) in comparison with the main targets (213,393 sources) of *Kepler*'s mission (density plot in black). The red marker represents the location of *Gaia EDR3 2077240046296834304* (see Section 4.2.3) that falls in the binary sequence.

3.3. Aperture Photometry

With the detailed PRF models computed from the FFI data for every channel and quarter combination we are able to evaluate them for every source in the EXBA images. We evaluate the PRF model on the Cartesian grid of pixel coordinates of the image data and with a maximum distance up to six pixels from the center of the source (obtained from the Gaia astrometry). The PRF model evaluation leads to a normalized (to sum 1) flux model of the source. In this work we evaluate the PRF model to obtain a normalized model of the sources aiming to capture the characteristic shape of the PRF, in contrast with the LFD photometry method where the evaluation aims to obtain the total flux of the source.

Following *Kepler*'s crowding and flux loss (CROWDSAP and FLFRCSAP respectively, Kinemuchi et al. 2012) metrics that the pipeline calculated for the photometric aperture of every primary target, we compute two equivalent metrics. Per definition, FLFRCSAP is the fraction of target flux contained in the photometric aperture over the total target flux. While CROWDSAP is the ratio of target flux relative to the total flux within the photometric aperture including contaminating sources. Therefore a CROWDSAP value of 1 means no contamination and a FLFRCSAP value of 1 means the aperture contains the entire flux of the source. Eval-

uating the PRF model for all sources and given their photometric aperture, we can compute both crowding and completeness metrics for every source.

We use isophotes to define the boundaries of the photometric apertures. The boundary of each isophote for a given source is defined by the flux value at a certain percentile of the normalized flux distribution. The seven percentiles are 0, 15, 30, 45, 60, 75 and 90. This leads to seven different apertures that follow the characteristic PRF shape and enclose different levels of flux completeness and contamination. Per definition, larger percentile values lead to smaller apertures and therefore less contamination (larger CROWDSAP values) but less flux completeness (smaller FLFRCSAP values). Additionally, we include an extra aperture in which the percentile that defines the isophote value is computed by simultaneously optimizing both metrics, FLFRCSAP and CROWDSAP. This scalar optimization is performed with *scipy*'s Brent's method⁷. After the target value is reached for either of the metrics, a softening term⁸ is applied to allow the optimization to focus in the second metric until both reach their respective target scores, instead of driving a single metric to the optimal point. We optimize the aperture size by targeting for a CROWDSAP > 0.8 and a FLFRCSAP > 0.5.

Providing multiple aperture photometry allows the users to choose the most suitable one depending on their scientific goal. Each aperture photometry has its associated FLFRCSAP and CROWDSAP metrics. Later, as indicated in *Kepler Archive Manual* (Thompson et al. 2016), crowding corrected fluxes can be computed by applying the following equation:

$$F_{corrected} = F - med(F)(1 - CROWDSAP) \quad (1)$$

where F is the original flux as provided in the light curve files, CROWDSAP is the crowding metric, and $med(F)$ is the median value of the uncorrected fluxes. Finally, both metrics can be used to stitch and adjust the light curves from different quarters to account for aperture variations due to changes in the PRF profile.

4. RESULTS

4.1. Data Products

⁷ https://docs.scipy.org/doc/scipy/reference/generated/scipy.optimize.minimize_scalar.html

⁸ We redefine the updated metric value as $metric' = target + leakFactor(metric - target)$ where the *target* is the desired target value for the metric (e.g. 0.9), *metric* is the current value, and *leakFactor* is a user defined value (e.g. 0.001).

In this work we produce two high-level data products. First, a data set of light curves with multiple aperture photometry for 9,327 sources observed by *Kepler* in the EXBA masks. We defined the multi-apertures as seven different isophote levels of the PRF model evaluated at every source. Secondly, a set of Python tools that allow the use of our precomputed PRF models to perform aperture photometry in any *Kepler*-like data, such as TPFs and the EXBA data.

The light curves provided in this work are stored at the MAST archive⁹ and can be accessed similarly as the main *Kepler*'s LCFs. Each FITS file contains light curves of a single EXBA source observed during a quarter. The FITS files are multi-extension, with a table containing the flux time series from multi-aperture photometry, and 8 extra image extension containing the aperture mask used for every photometric aperture. There are a total of 90,224 LCFs, which accounts for the number of observed sources and the number of quarters each source was observed. Each file header contain relevant keywords such as Gaia's source information, EXBA origin file, and the completeness and contamination metrics for all the photometric apertures. Alongside the LCFs, a catalog with all observed Gaia sources for each channel and quarter is also available. Appendix A details the structure and content of each EXBA LCF.

Accompanying this dataset of light curves we release `kepler-apertures`¹⁰, a Python library that allows to reproduce the results presented in this work. The PRF models computed from *Kepler*'s FFIs are included in the library. Through using the this PRF models users can build aperture masks and compute flux metrics for any type of *Kepler*'s prime mission data. `kepler-apertures` also provides the functionalities to compute new PRF models from FFI data by using the LFD method.

4.2. Finding Transiting Signals

As planned, the *Kepler* pipeline only produced TPFs for the EXBA mask and no light curves were extracted. Thus, the EXBA data has never been systematically analyzed to search for exoplanet candidates, or any other time domain studies. We follow a standard approach to search for transiting signals.

4.2.1. Detrending

Before analyzing each light curve for scientific purposes, we process them to correct for instrumental ef-

fects. Not only that, numerous stars show stellar activity due to rotation or pulsation, these signals need to be removed to isolate small variations of the incoming flux originated from transit events. Removing these types of signals is often refer as detrending.

We use the Cotrending Basis Vectors (CBVs, [Smith et al. 2012](#)) to account for the systematic signals introduced by the instrument. CBVs are a series of 16 basis vectors that capture most of the known correlated features in a reference ensemble of flux time series. The *Kepler* pipeline computed these basis vectors for every quarter and output channel combination. As shown in [Smith et al. \(2012\)](#), the first 8 CBV components capture most of the systematic errors, therefore for this work we only use the first eight basis vectors. To capture variability due to stellar activity, such as rotation or pulsation, we use a set of basis splines. Similar to [Vanderburg & Johnson \(2014\)](#) we found that the number of knots for the spline basis equivalent to a spacing of 1 day allows fitting variability in short time scales without losing transit-like signals. Combining the aforementioned set of basis vectors we defined a design matrix that is fitted using linear regression to the data and obtain the corrected time series. We perform this detrending correction for all the source light curves on a per quarter basis. As an example, Figure 5 shows the flux time series of *Gaia* EDR3 2077240046296834304. The light curve corrected only with the CBVs (upper panel) shows clear stellar variability in the scale of days. The light curve after full detrending (middle panel) preserves the transiting signal. Although the fully corrected light curve still shows residual stellar variability (as seen in the 1 day binned light curve shown in black), the amplitude is significantly smaller than the transiting signal.

4.2.2. Box Least Square Periodogram

We perform a search for periodic transiting signals using the Box Least Square Periodogram (BLS, [Kovács et al. 2002](#)). The BLS method searches for periodic variability by fitting the data with an upside-down top hat periodic model. The model is parameterized by the period, transit duration, and the time at mid-transit.

Due to the structure of our light curves, which are separated by quarters, we compute the BLS periodograms in two time regimes. First, on a per quarter basis search using a grid periods between 0.2 and 30 days. The grid consist in 60,000 values evenly spaced in frequency. The upper limit allows for detecting at least three transits within the ~ 90 days time window of each quarter. Secondly, we search for signals with periods ranging from 60 to 360 days, for this we use the object light curves from

⁹ Kepler Bonus, APEXBA, <https://doi.org/10.17909/t9-d5wy-e535>

¹⁰ <https://github.com/jorgemarpa/kepler-apertures/releases/tag/v0.1.0>

all available quarters. The BLS periodogram return us the parameters of the model that best fits the data.

To remove periodic signals originated from high-amplitude eclipsing binary systems and other types of periodic pulsators we filtered the BLS parameters results. This filtering isolates transiting signal potentially originated from small companions. We only consider sources with the following BLS results: 1) transit depth lower than 10% in normalized flux units, 2) a signal-to-noise ratio of the periodogram maximum power larger than 20, and 3) a periodogram maximum power larger than 20 after standardizing the periodogram by the mean and standard deviation of the ensemble of periodograms.

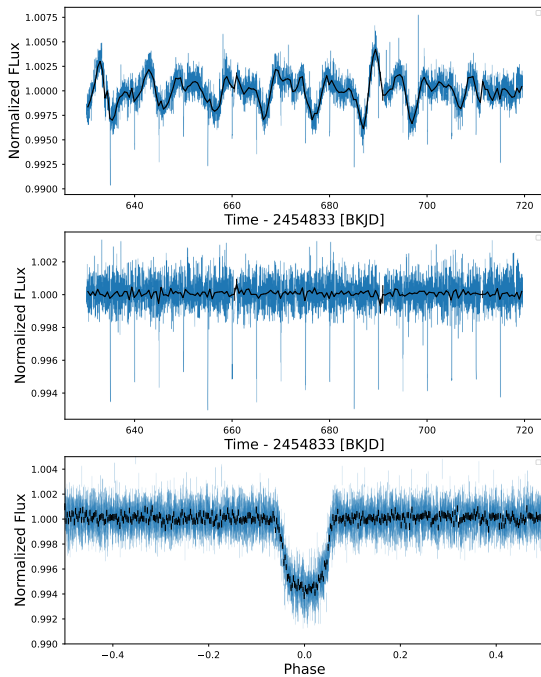


Figure 5. Time-based light curve (top two panels) and phase-folded light curve (bottom panel) of *Gaia EDR3 2077240046296834304*. Blue markers are the flux measurements, while black markers are the binned light curves using a time bin size of 1 day for the time light curve. The top and middle panels show the CBV-only corrected and fully detrended (CBVs and splines) light curves both respectively, for observations during quarter 7. The phase-folded light curve contains data from all quarters as described in Section 4.2.3. The transit u-like shape and depth ($\sim 0.5\%$) evidence the possibility of a large planet candidate or a sub-stellar companion. The parameters that characterize the best transit model are listed in Table 1.

After a visual inspection of less than two hundred light curves after the aforementioned filtering, one source stands out. *Gaia EDR3 2077240046296834304* (here and after *G...304*) exhibits the characteristic transit

shape and depth of a large planet or a sub-stellar companion. Figure 5 shows both time-based (quarter 7) and phase folded light curve of *G...304*.

4.2.3. *Gaia EDR3 2077240046296834304*

G...304 was observed in the EXBA masks during quarters 7, 8, 11, 12, 15, and 16, and it is located outside the coverage of the mask (within 1 pixel from the mask border) according to Gaia astrometry. Moreover, it was also observed as a background source in the main TPF of KIC 7214804 continuously between quarters 2 and 17. As shown in Figure 6, Gaia astrometry (solid red dot in the figure) locates *G...304* inside the TPF, but sufficient flux is contained in the EXBA data to detect the transit events.

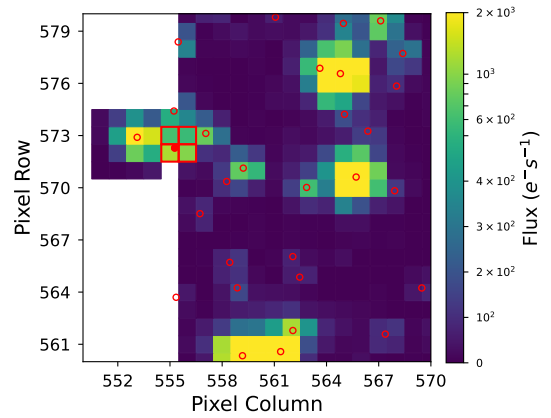


Figure 6. Image in pixel space of the EXBA data (Pixel Column ≥ 556) and the KIC 7214804 TPF (Pixel Column < 556) where the host candidate *Gaia EDR3 2077240046296834304* is located. The flux data is an average of cadences observed during quarter 7. Red circles show Gaia EDR3 sources, while the solid circle locates the host candidate. The red squares illustrate the aperture mask used for this work.

Because the EXBA masks did not capture *G...304* during quarters 2 through 6, 9, 10, 13, 14, and 17, we decided to work only with quarters that have both EXBA and TPF data. Combining the EXBA and TPF pixel data we are able to create a "stitched" pixel image which improves flux completeness leading to a more accurate photometry. Not using all available quarters does not impact the number of observed transits in a significant amount and allows to obtain accurate model fitting. We compute a new photometric aperture from the combined image that maximizes the transiting signal using the `contaminante`¹¹ (Hedges et al. 2021b) Python

¹¹ <https://github.com/christinahedges/contaminante>

package. Given a period value and transit reference time, `contaminante` creates an aperture mask by finding which pixels contain the transiting signal at high significance, marginalizing over known instrument systematics.

We defined the orbital parameters of *G...304* using the BLS algorithm at a finer period grid. We found a transit period of 4.99667 days, a transit reference time of 2455468.058 Julian days, a duration of 0.091 days, and a normalized transit depth of 0.005. An odd-even transit depth test (Wu et al. 2010) helps to separate transit signals originated from eclipsing binaries. We perform this test with the best BLS model parameters resulting in a test statistic value of 0.00235 and significance level of 96.17% indicating the odd and even transits are statistically consistent. The transiting signal is a viable case for a transiting planet (see Figure 5, lower panel), with a transit-like shape and a transit depth consistent with a large planet or sub-stellar companion. *G...304* light curve also evidences significant variability due to stellar activity in the scale of days.

Unfortunately, Gaia DR2 and EDR3 do not provide estimates of the stellar radius, luminosity, or line-of-sight extinction for *G...304*, only an estimate of the effective temperature ($T_{eff} = 4,358$ K). To constrain the host star parameters and understand the evolutionary state of *G...304*, we perform a spectral energy distribution (SED) analysis of the available Gaia (G , B_P , and R_P , (Gaia Collaboration et al. 2018)), 2MASS (J_{2M} , H_{2M} , and K_{2M} (Cutri et al. 2003)), and WISE (W1 and W2, Cutri & et al. 2012) photometry using the publicly available exoplanet fitting suite, EXOFASTv2 (Eastman et al. 2013, 2019). We included the MESA Isochrones and Stellar Tracks (MIST) stellar evolution models (Paxton et al. 2011, 2013, 2015; Choi et al. 2016; Dotter 2016) within the fit to precisely estimate the host star parameters. A Gaussian prior on the parallax from Gaia DR2 of 1.05010 ± 0.22882 mas (corrected for the $-30 \mu\text{as}$ offset reported by Lindgren et al. (2018) was enforced on the fit and we also include an upper limit of 0.6677 mag on the line-of-sight extinction (A_V) from Schlegel et al. (1998) & Schlafly & Finkbeiner (2011). Lastly, we assume a solar metallicity prior of 0.0 ± 0.25 dex. Our analysis showed that *G...304* is a K-dwarf star with a mass of $0.749 M_\odot$, a stellar radius of $0.720 R_\odot$, effective temperature of 4,410 K consistent with the value provided by Gaia DR2, and a density of 2.83g/cm^3 . Table 1 summarizes these results.

We model the light curve of *G...304* using the exoplanet library (Foreman-Mackey et al. 2021) and `pymc3` (Salvatier et al. 2016). These tools allow to set priors for the stellar parameters, such as the stellar ra-

dius (R_*), density (ρ_*) and Limb Darkening, and for the orbital parameters such as period (P), transit reference time (t_0), impact parameter (b) and the ratio between the planet and the star (R_p/R_*). In a similar manner as Sandford & Kipping (2017) and including the stellar parameter results from the SED fitting for this system, we adopt the following priors:

- t_0 : a uniform prior bounded by $t_{0,\text{BLS}} - 0.5$ days and $t_{0,\text{BLS}} + 0.5$, where $t_{0,\text{BLS}}$ is the transit time at maximum power from the BLS periodogram.
- P : a uniform prior from $0.9P_{\text{BLS}}$ to $1.1P_{\text{BLS}}$ days, where P_{BLS} is the period at maximum power from the BLS periodogram.
- b : a uniform prior from 0 to 2.
- R_p/R_* : a uniform prior from 0 to 1.
- quadratic Limb Darkening coefficients, u_1 and u_2 , following the uninformative prior defined by Kipping (2013).
- ρ_* : reparameterized as $\log_{10}(\rho_* [\text{kg/m}^3])$ and a uniform prior in log space between 0 and 3.5, which is the stellar density from the SED fitting in units of $[\text{kg/m}^3]$.
- $R_{*,\text{SED}}$: a uniform prior between 0 and $1.1R_{*,\text{SED}}$.

G...304 locates close to the binary sequence in the HR diagram (red marker in Figure 4) and has a large value of Gaia's Renormalized Unit Weight Error (RUWE = 4.2)¹² suggesting that the target could be an unresolved binary system. Considering the relation between the RUWE and the photocentre perturbation derived by Belokurov et al. (2020), *G...304* has a centroid perturbation of ~ 2 mas (~ 2 AU at 970 pc distance). Considering a physically possible binary systems with a K-dwarf primary (as the SED fitting suggested) and a K-dwarf (or a smaller M-dwarf) secondary with a 5-day period orbit and an estimated 0.065 AU semi-major axis (assuming non-eccentric Keplerian orbit) can not account for a 0.5% transit depth and the measured astrometric scatter. Therefore, the transits must be produced by a third body orbiting one of the stars in the binary system. We added a dilution term to our light curve model that accounts for the flux provided by a companion following the parametrization suggested by Espinoza et al. (2019):

¹² https://gea.esac.esa.int/archive/documentation/GDR2/Gaia_archive/chap_datamodel/sec_dm_main_tables/sssec_dm_ruwe.html

$$\mathcal{M}(t) = [\mathcal{T}(t)D + (1 - D)] \left(\frac{1}{1 + DM} \right) \quad (2)$$

where $\mathcal{T}(t)$ is the transit model defined by the stellar and orbital parameters, D is the dilution term, and M is the out-of-transit target flux.

The results of the model fitting are presented in Table 1 while the joint posterior distributions are shown in Figure 7. The inferred parameters for the radius $0.81^{+0.54}_{-0.54}R_J$ of the candidate (with a maximum radius of $2.2R_J$ from the posterior distribution), indicate the transits are produced by a substellar companion orbiting at 0.034 AU. Subtracting the most representative model to the data shows no remaining signal, as shown in Figure 8. The inferred stellar density ($2.60g/cm^3$) is in agreement (within the errors) with the value obtained from the SED fitting. The mean value in the stellar parameters inferred from the model fitting ($R_* = 0.4 \pm 0.26R_\odot$ and $M_* = 0.116^{+0.54}_{-0.11}M_\odot$) differ with those found from the SED fitting ($R_{*,SED} = 0.720^{+0.048}_{-0.046}R_\odot$ and $M_{*,SED} = 0.749^{+0.048}_{-0.049}M_\odot$) due to the inclusion of the dilution term. During the SED fitting, we treated the target as a single star. Including the dilution term also affected the width of the posterior distributions, enlarging the derived uncertainties for stellar radius and mass.

4.3. *Eclipsing Binaries*

The EXBA masks were designed and observed to estimate the unbiased occurrence fraction of EBs in the Kepler field. Although in this work we do not pursue a thorough and complete search of this type of variables, during the exoplanet search previously describe we found many EBs. Here we present a catalog of EBs and their eclipsing parameters derived from the BLS periodogram. Table 2 lists 69 EB systems found in the EXBA masks. The model parameters period, transit depth, reference time, and duration are derived from the best BLS fitting. We perform a visual inspection to remove clear contaminated sources and a cross-reference search with the literature (Simbad search). The two types of EBs are present in this catalog. One of them are contact systems (EWs, see Figure 9) where both components are in contact and sharing a common envelope. EWs have light curves in which both minima are of similar depth and their typical periods are shorter than a day showing large-amplitude variability. The second type are detached systems (EAs, see Figure 9), where both components are of different spectral type. Therefore, both the primary and secondary minima have different depths, and the beginning and end of the eclipses are

typically very well defined. EAs are the major source of contamination when searching for exoplanets using the transiting method.

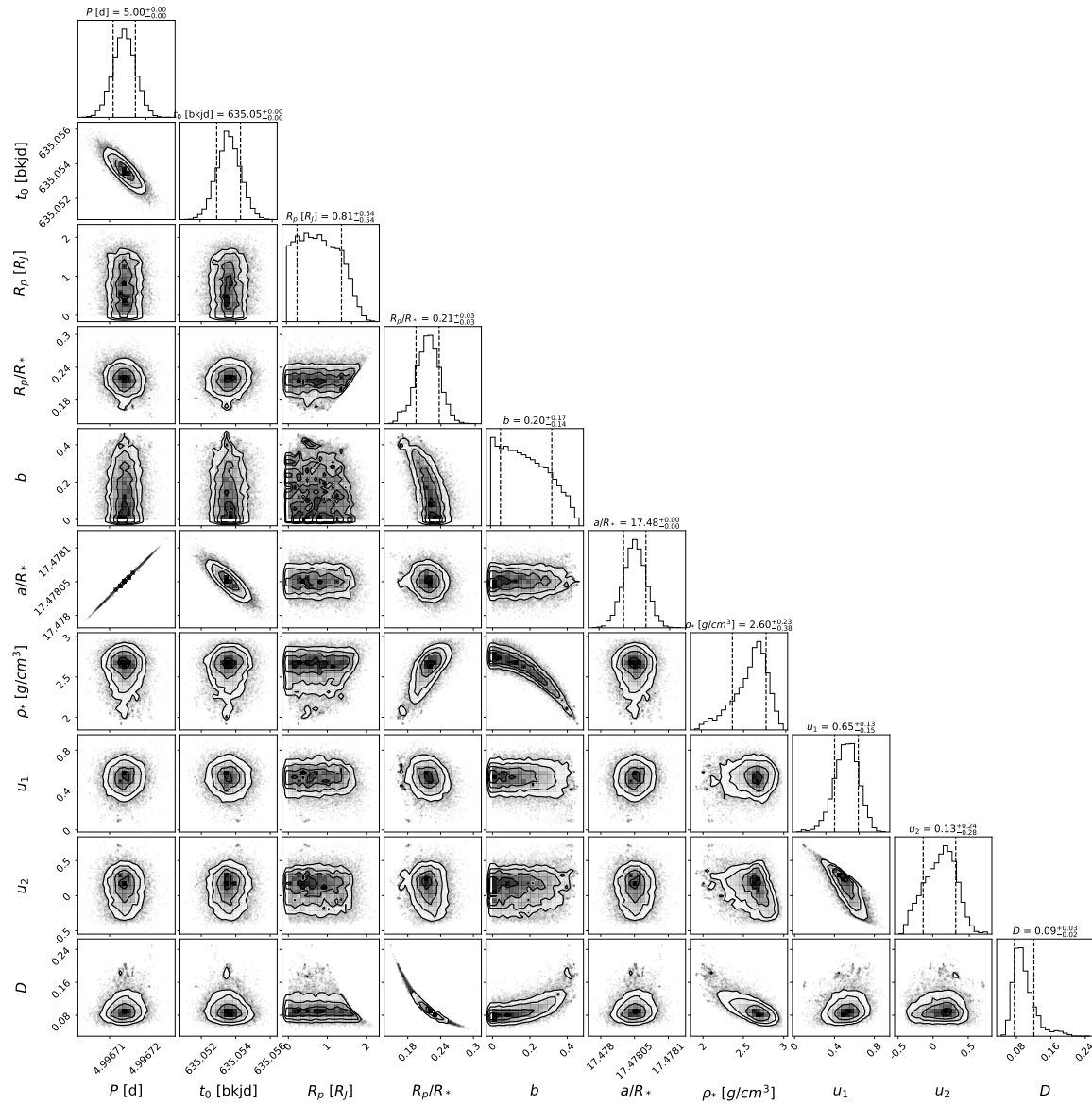


Figure 7. Posterior distributions of inferred stellar and transit parameters for the transiting signal observed around *Gaia* EDR3 2077240046296834304. The model fitting was performed using the `exoplanet` Python package following the priors described in Section 4.2.3. The posteriors suggest the eclipse signal is produced by a large planet with a radius $< 2R_J$.

Table 1. Best model parameters from the SED fitting (first block) and the transiting signal fitting using the `exoplanet` library (second and third block) around *Gaia* EDR3 2077240046296834304. The last block details the host Gaia EDR3 values.

Parameter	Description	Value
$R_{*,\text{SED}}$..	Radius [R_{\odot}]	$0.720^{+0.048}_{-0.046}$
$M_{*,\text{SED}}$..	Mass [M_{\odot}]	$0.749^{+0.048}_{-0.049}$
L_*	Luminosity [L_{\odot}]	$0.175^{+0.044}_{-0.034}$
$\rho_{*,\text{SED}}$...	Stellar density [g/cm^3]	$2.83^{+0.48}_{-0.40}$
$\log(g)$...	Surface gravity [cm/s^2]	4.598 ± 0.04
$T_{\text{eff,SED}}$..	Effective Temperature, SED [K]	4410^{+150}_{-140}
[Fe/H] ...	Metallicity (dex)	$0.32^{+0.15}_{-0.18}$
R_*	Radius [R_{\odot}]	$0.400^{+0.26}_{-0.26}$
M_*	Mass [M_{\odot}]	$0.116^{+0.39}_{-0.11}$
ρ_*	Stellar density [g/cm^3]	$2.60^{+0.23}_{-0.38}$
u_1	Limb Darkening Coefficient 1	$0.65^{+0.13}_{-0.15}$
u_2	Limb Darkening Coefficient 2	$0.13^{+0.24}_{-0.28}$
D	Dilution	$0.09^{+0.03}_{-0.02}$
R_P	Radius [R_{Jup}]	$0.81^{+0.54}_{-0.54}$
P	Period [days]	$4.99671123 \pm 4.66 \times 10^{-6}$
t_0	Transit Mid Point [BKJD]	635.0541 ± 0.0005
t_{14}	Duration [hours]	$0.1 \pm 1 \times 10^{-6}$
b	Impact parameter	$0.2^{+0.17}_{-0.14}$
a	Semi-Major Axis [AU]	$0.032^{+0.02}_{-0.02}$
a/R_*	Semi-Major Axis / R_*	$17.48 \pm 1 \times 10^{-5}$
α_{J2000} ...	R.A.	295.859489 ± 0.000132
δ_{J2000} ...	Decl.	42.713179 ± 0.000142
μ_{α}	Proper Motion RA [mas/yr]	-1.99 ± 0.17
μ_{δ}	Proper Motion Dec [mas/yr]	-9.40 ± 0.20
π	Parallax [mas/yr]	1.03 ± 0.15
$T_{\text{eff,Gaia}}$..	Effective Temperature, Gaia DR2 [K]	$4358.5^{+244.7}_{-351.5}$
G	Gaia EDR3 G magnitude	16.5922
R_P	Gaia EDR3 R_P magnitude	15.6498
B_P	Gaia EDR3 B_P magnitude	17.2516

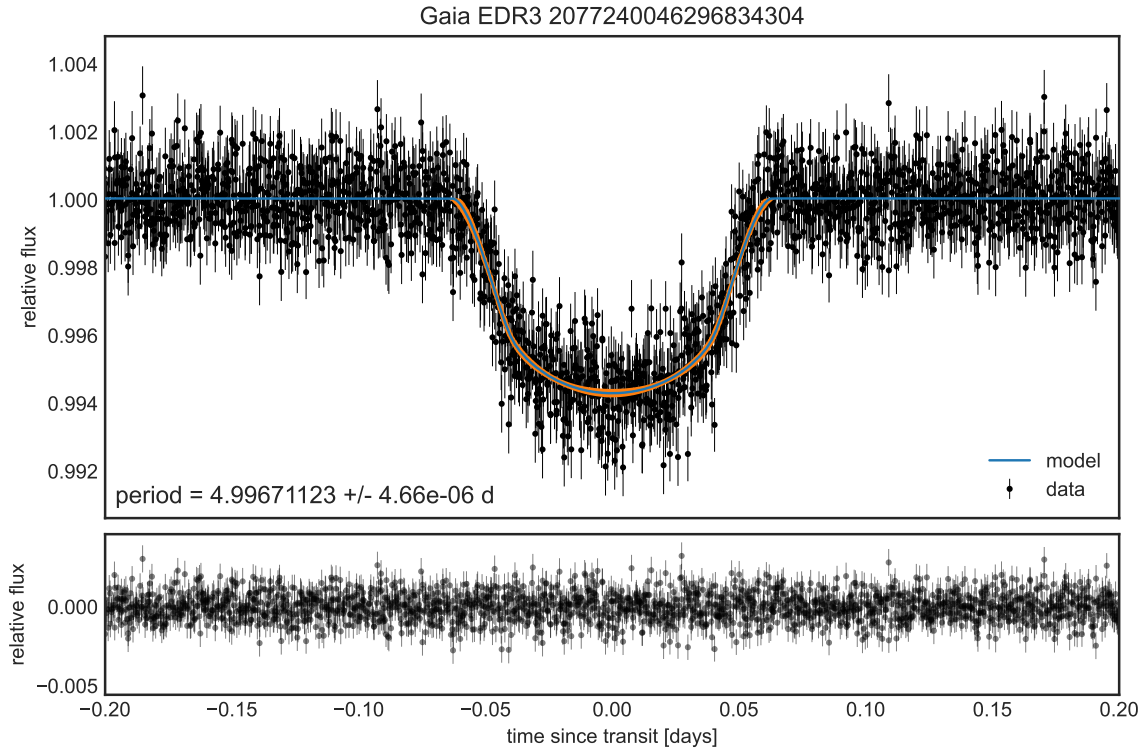


Figure 8. Transit model fitted using the `exoplanet` tool. The upper panel shows the light curve data (black markers), the median model (solid blue line), and the 3rd and 97th percentile (in orange) from the posterior distribution. Residuals are shown in the lower panel with no clear evidence of a remaining signal. The transit shape and depth are typical of a large planet companion.

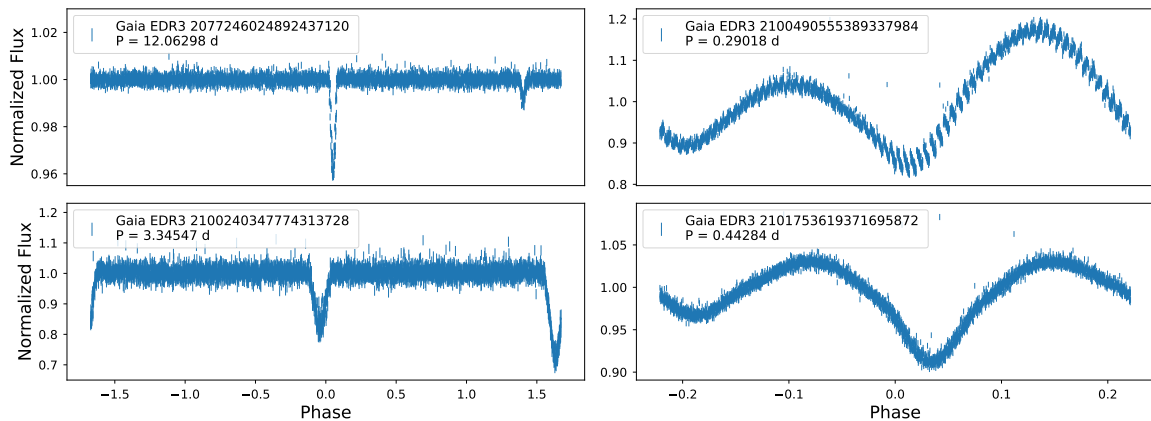


Figure 9. Examples of Eclipsing Binaries found in *Kepler*'s EXBA masks. Detached systems (EAs) show well defined primary and secondary eclipses and are the major source of false positive when looking for exoplanet candidates. Contact systems (EWs) show continuous eclipses and typically have shorter periods than detached EBs.

Table 2. Catalog of 69 Eclipsing Binary systems found in the EXBA masks. This EB catalog represents an incomplete search for this type of variables and is only presented as an illustration of the opportunities that this data presents. These EBs are a result of a search for periodic transiting signal limited to periods between 0.2 and 100 days and with a standardized periodogram peak value larger than 20, see Section 4.2.2 for further details.

Gaia ID	Period days	$BKJD_0$ days	Duration days	Depth %
Gaia EDR3 2051774184464360064	0.816420	443.893508	0.099	1.030747
Gaia EDR3 2051871182004752512	0.531408	443.762933	0.450	2.848130
Gaia EDR3 2052499488484831616	0.523529	630.445491	0.450	6.528912
Gaia EDR3 2052503164977145088	0.551766	443.795923	0.450	0.104680
Gaia EDR3 2052503164977145472	0.551766	443.795923	0.450	12.661261
Gaia EDR3 2052524429346526464	0.969631	540.414513	0.099	9.448619
Gaia EDR3 2053614118393506176	0.532076	443.725578	0.099	18.842998
Gaia EDR3 2053614182812468480	0.532076	443.725578	0.099	0.997837
Gaia EDR3 2073608428123884416	0.707867	443.657609	0.150	0.096724
Gaia EDR3 2073608462478158848	2.006032	445.105109	0.099	0.198396
Gaia EDR3 2073608462483635968	2.006032	445.105109	0.099	0.205073
Gaia EDR3 2073682438989499392	0.707867	443.660681	0.126	0.056299
Gaia EDR3 2073682438989966592	0.707867	443.660681	0.126	0.042618
Gaia EDR3 2073682640842559360	0.707867	630.538708	0.126	5.968305
Gaia EDR3 2073682645147919616	0.707867	443.840681	0.450	7.558699
Gaia EDR3 2075404789599593088	3.034506	444.869691	0.330	2.204107
Gaia EDR3 2075405133185880704	0.541367	443.837691	0.450	0.821595
Gaia EDR3 2075405133185894656	0.541367	443.837691	0.450	0.230565
Gaia EDR3 2075406541944219520	0.630683	443.765691	0.450	0.072754
Gaia EDR3 2076208292075451136	0.646481	443.890268	0.399	0.829846
Gaia EDR3 2076209357217808384	0.618034	443.722268	0.399	5.536100
Gaia EDR3 2076209456001789056	6.810999	445.073768	0.150	1.027946
Gaia EDR3 2076505018468886784	0.542118	443.714849	0.450	0.707253
Gaia EDR3 2076789723264283008	13.362883	446.483764	0.450	1.503108
Gaia EDR3 2076789727566520192	3.524663	445.685764	0.450	0.800765
Gaia EDR3 2076836727387736576	3.554231	542.873966	0.201	2.813851
Gaia EDR3 2076836864825475456	0.707867	443.663764	0.126	1.174416
Gaia EDR3 2077245814431169792	0.637804	630.807001	0.051	32.182456
Gaia EDR3 2077246024892437120	12.062975	445.235872	0.450	0.831434
Gaia EDR3 2077810555389602176	0.604800	539.753960	0.399	2.754031
Gaia EDR3 2078117181696007296	0.983511	444.397464	0.099	11.280642
Gaia EDR3 2078734140854317440	0.525966	735.642432	0.450	6.108658
Gaia EDR3 2078735858841858816	2.414770	445.490808	0.174	1.672115
Gaia EDR3 2079019292324040704	0.628500	443.743214	0.051	1.849365

Table 2 *continued*

Table 2 (*continued*)

Gaia ID	Period	$BKJD_0$	Duration	Depth
	days	days	days	%
Gaia EDR3 2079399006085883008	11.236515	446.155307	0.099	1.319522
Gaia EDR3 2080297753770786944	2.170456	443.921954	0.126	1.089285
Gaia EDR3 2080297753770788864	0.827853	444.160454	0.051	4.862135
Gaia EDR3 2082091568328182528	0.701906	443.740152	0.051	2.486457
Gaia EDR3 2086516449796423936	2.632309	443.777988	0.174	18.155153
Gaia EDR3 2086516454099067776	2.632309	443.780988	0.126	0.191745
Gaia EDR3 2086592354758573568	6.359473	444.454549	0.399	1.276964
Gaia EDR3 2100240347774313728	1.672736	443.540000	0.099	10.979652
Gaia EDR3 2100490555389337984	0.580361	443.824932	0.051	11.126328
Gaia EDR3 2101033920292227584	3.734361	447.016742	0.051	6.638635
Gaia EDR3 2101136415390982528	0.752610	443.745168	0.450	1.506718
Gaia EDR3 2101136419694167040	0.752610	443.754168	0.450	1.984499
Gaia EDR3 2101752936479788544	0.552366	443.755662	0.051	9.413652
Gaia EDR3 2101753516292218624	0.530687	443.817162	0.450	7.978087
Gaia EDR3 2101753520591885568	0.530687	443.817162	0.450	7.094880
Gaia EDR3 2101753619371695872	0.885682	444.205662	0.099	4.122006
Gaia EDR3 2102900959754861440	1.481648	443.734874	0.099	3.322106
Gaia EDR3 2103827298302304128	0.533752	539.746877	0.450	1.101425
Gaia EDR3 2104814389164263168	0.595171	443.855354	0.051	4.316045
Gaia EDR3 2106327622103110784	20.544483	463.879921	0.450	5.975260
Gaia EDR3 2107265956496766208	0.604584	443.898714	0.450	5.087825
Gaia EDR3 2107266536313762816	1.640355	444.341214	0.099	12.684281
Gaia EDR3 2126083788772171648	0.608346	539.695481	0.450	0.021125
Gaia EDR3 2126085369316699648	0.601366	539.876981	0.399	2.233859
Gaia EDR3 2126085369320144640	0.841974	539.699981	0.051	3.655029
Gaia EDR3 2126955323535081728	0.608346	539.695419	0.450	16.312343
Gaia EDR3 2127956149696086272	0.601936	539.759749	0.399	1.934922
Gaia EDR3 2127957734541969152	0.658113	443.884613	0.051	10.867783
Gaia EDR3 2128160285200885888	0.562013	443.844143	0.450	5.224848
Gaia EDR3 2128267968619535872	0.515723	443.959706	0.051	0.231262
Gaia EDR3 2128268587094813056	0.585238	443.715206	0.450	1.411582
Gaia EDR3 2129514093249096832	0.875163	444.168417	0.450	1.554462
Gaia EDR3 2130912843839236224	25.235131	460.013006	0.249	3.355718
Gaia EDR3 2133602451140200192	0.985036	444.216754	0.174	2.357031
Gaia EDR3 2134814804448660608	0.707178	444.006163	0.150	10.898769

NOTE—The $BKJD_0$, duration, and depth are the results from the best BLS model and account for the primary eclipse. The $BKJD_0$ correspond to the Barycentric Kepler Julian Day ($BKJD = BJD - 2,454,833.0$). These parameters were obtained from fitting the BLS model with a broad period and duration grid, therefore are not necessarily the most accurate results.

5. DISCUSSION

In this section, we will discuss the relevant assumptions of our work as well as its limitations.

The use of custom apertures that follow the PRF shape becomes important when its profile are elongated and a significant fraction of the flux falls in the wings of the profile. Elongated PRF profiles are particularly true for *Kepler* as we move away from the center of the focal plane (see Figure 2). Although these aperture masks are more complex than standard circular-like apertures, photometry in crowded regions where multiple sources are located within pixel distance is sub-optimal. Under these circumstances, PSF/PRF photometry is recommended, such as the LFD photometry method. Nonetheless, for isolated sources, custom apertures represent a fast and accurate method to extract their photometry.

As discussed in Hedges et al. (2021a), fitting the PRF model follows a series of assumptions. Two of them are relevant to our work: the PRF does not change with time during each quarter and is uniform across each channel. Both assumptions are reasonable up to some limit, the PRF shape can suffer changes in time due to focus recalibration of the instrument and spatially within a channel.

The time dependency can be mostly corrected using the CBVs as they capture the instrument systematics. Another approach is to introduce a time dependency to the PRF model, although this can not be done using *Kepler*'s FFIs due to their limited observing cadence. This strategy is feasible if using *Kepler*'s clusters apertures (e.g. NGC 6819), where the number of sources is high enough to provide a smooth PRF model ($\sim 2,000$ sources and $\sim 40,000$ pixel data points) and the observed cadence is in long mode (~ 4400 cadences).

The PRF profile can slightly change across a single channel, these variations are averaged when estimating the shape model for the full CCD. As the typical scale of a PRF model is < 4 pixels and its variations within the channel happen at a smaller scale (1 to 2 pixels), the effect in the photometric apertures defined from the PRF profile is minimal, especially for the small size of the EXBA masks (36 x 60 pixels) compared to the FFIs (1,024 x 1,100 pixels). If needed, the spatial change of the PRF profile can be model by including a spatial dependency to the PRF model or by dividing the channel image into a grid where each cell contains a dedicated model of the PRF.

The catalog of light curves for 9,327 sources presented in this work is based on a Gaia search done at a limiting magnitude of $G = 20$. Thus, fainter sources not only do not have time series but also are not considered for contamination metrics. This sets the CROWDSAP met-

ric reported in this work as an upper limit, but the flux contribution from sources fainter than 20th magnitude is minimal in *Kepler* observations. The Gaia search could be relaxed in future works to allow fainter sources.

6. SUMMARY

In this work, we extracted source light curves from *Kepler*'s EXBA masks for the first time. The EXBA masks are a set of custom masks observed by *Kepler* during its prime mission between quarters 5 and 17, which has never been analyzed before. We created light curve files for 9,327 Gaia sources observed in the EXBA masks. In our processing pipeline, we used the method described in the LFD photometry (Hedges et al. 2021a) to model the PRF profile of all channels using *Kepler*'s full frame images. We capitalized on the large number of sources observed in these FFIs ($\sim 10,000$ per channel) to obtained detailed PRF models. We evaluated the PRF models for every source in the EXBA masks to define photometric aperture. These aperture masks follow the characteristics shapes of the PRF and enabled to compute flux completeness and crowdedness metrics. The light curves files produced in this work are available for public access through the MAST archive. The PRF profile models built from the FFIs are a sub-product of our work. The Python library `kepler-apertures` enables user to utilize our precomputed PRF models (included in the package) to perform aperture photometry on *Kepler* like data.

As an example of what can be accomplished with these high-level science products, we present two scientific cases. First, we find evidence of an exoplanet candidate around *Gaia* EDR3 2077240046296834304. The results of the transit model fitting suggest that the object producing this transit has a size smaller than $2.2R_J$. Further investigations need to be conducted to constrain the stellar properties of the host as well as the parameters of the transiting objects in order to confirm its planetary nature. As a second case, we presented a catalog of Eclipsing Binaries found during the search for transiting signals. The EXBA masks were designed with the primary purpose of estimating the fraction of background EBs systems in the *Kepler* field. EBs are the major source of false positives when searching for exoplanets. Although in this work we did not attempt a complete search of EBs, we found a significant number (69) of them and compute its basic parameters using the BLS periodogram. A more thorough search and analysis of the EXBA light curves to estimate the occurrence fraction of EBs is left to the community.

This work presents the tools to perform aperture photometry of *Kepler* data in a similar fashion as the *Kepler*

pipeline and provides to the community a new dataset that has not been systematically explored yet. This methodology can be applied systematically to all the background sources found in the *Kepler* targets, which are estimated to contain more than 129,000 sources. Although a large fraction of them are blended sources and a fully PSF photometry approach is more suitable (e.g. LFD photometry), numerous of these sources are isolated, and fast aperture photometry is the optimal approach. Even more, the *K2* mission shares similar data characteristics as *Kepler*'s prime mission and the application of these tools extends naturally.

This paper includes data collected by the Kepler mission and obtained from the MAST data archive at the Space Telescope Science Institute (STScI). Funding for the Kepler mission is provided by the NASA Science Mission Directorate. STScI is operated by the Association of Universities for Research in Astronomy, Inc., under NASA contract NAS 5-26555. This work has made use of data from the European Space Agency (ESA) mission Gaia (<https://www.cosmos.esa.int/gaia>), processed by the Gaia Data Processing and Analysis Consortium (DPAC, <https://www.cosmos.esa.int/web/gaia/dpac/consortium>). Funding for the DPAC has been provided by national institutions, in particular the institutions participating in the Gaia Multi-lateral Agreement. This research made use of exoplanet (Foreman-Mackey et al. 2021) and its dependencies (Astropy Collaboration et al. 2013, 2018; Kipping 2013; The Theano Development Team et al. 2016; Salvatier et al. 2016; Luger et al. 2019; Kumar et al. 2019; Agol et al. 2020; Foreman-Mackey et al. 2021). Funding for this work for JMP and CH is provided by grant number 80NSSC20K0874, through NASA ROSES.

Facilities: Kepler

Software: astropy (Astropy Collaboration et al. 2013), lightkurve (Lightkurve Collaboration et al. 2018), scipy (Virtanen et al. 2020), psfmachine (Hedges & Martínez-Palomera 2021), kepler-apertures (Martínez-Palomera 2021), numpy (Harris et al. 2020), exoplanet (Foreman-Mackey et al. 2021), pymc3 (Salvatier et al. 2016), contaminante (Hedges et al. 2021b),

APPENDIX

A. EXBA LIGHT CURVE FILES

Each EXBA Light Curve File (LCF) contains the light curve of a single source and the aperture masks used for the photometry of a single quarter. Each LCF is named under the following pattern `hlsp_kbonus-apexba_kepler_kepler_<gaia_source_id>-q<quarter>_kepler_v1.0_lc.fits` where the fields are the Gaia EDR3 *source id* and the quarter number, respectively. Each LCF is a multi-extension FITS file that contains the following:

- The primary header unit. This extension contains the main metadata necessary to identify the object.
- The LIGHTCURVE extension. A binary table header unit containing the flux time series information. The columns of the table are detailed in Table 3.
- The APERTURE extensions. Eight image header units containing the aperture masks used for the eight different apertures as described in Section 3.3: first an optimized aperture (0) and then 7 apertures with decreasing size

as percentile increase. Each aperture mask matches the shape of the 4 tiled EXBA masks (36 x 60 pixels) for a given channel.

Accompanying the EXBA LCFs for a given quarter and channel combination, there are the `hlsp_kbonus-apexba_kepler_kepler_exba-mask-ch<channel>-q<quarter>_kepler_v1.0_sup.fits` files. These are support files used for plotting purposes. Each file contains three extensions:

- The primary header unit containing basic information of the EXBA mask such as center R.A. and Dec coordinates and pixel reference position.
- An image header unit with an averaged image across cadences of the tiled EXBA mask (36 x 60 pixels).
- A binary table unit containing the Gaia EDR3 catalog of sources observed in the EXBA mask.

Table 3. Description of the columns available in the Binary Table header unit containing the flux time series of sources in every EXBA Light Curve File.

Column	Field	Format	Units	Description
1	Time	float32	BJD - 2454833	Time value.
2	Cadenceno	int64	-	Cadence number.
3	Flux	float32	e^-/s	Flux from the optimized aperture.
4	Flux0	float32	e^-/s	Flux from the 1st aperture at percentile 0.
5	Flux15	float32	e^-/s	Flux from the 2nd aperture at percentile 15.
6	Flux30	float32	e^-/s	Flux from the 3rd aperture at percentile 30.
7	Flux45	float32	e^-/s	Flux from the 4th aperture at percentile 45.
8	Flux60	float32	e^-/s	Flux from the 5th aperture at percentile 60.
9	Flux75	float32	e^-/s	Flux from the 6th aperture at percentile 75.
10	Flux90	float32	e^-/s	Flux from the 7th aperture at percentile 90.
11	Flux_err	float32	e^-/s	Flux error from the optimized aperture.
12	Flux_err0	float32	e^-/s	Flux error from the 1st aperture at percentile 0.
13	Flux_err15	float32	e^-/s	Flux error from the 2nd aperture at percentile 15.
14	Flux_err30	float32	e^-/s	Flux error from the 3rd aperture at percentile 30.
15	Flux_err45	float32	e^-/s	Flux error from the 4th aperture at percentile 45.
16	Flux_err60	float32	e^-/s	Flux error from the 5th aperture at percentile 60.
17	Flux_err75	float32	e^-/s	Flux error from the 6th aperture at percentile 75.
18	Flux_err90	float32	e^-/s	Flux error from the 7th aperture at percentile 90.
19	Quality	int64	-	Quality flag from the TPF.
20	SAP_Quality	int64	-	Quality flag introduced by <code>lightkurve.KeplerLightCurve</code> .

REFERENCES

- Agol, E., Luger, R., & Foreman-Mackey, D. 2020, The Astronomical Journal, 159, 123, doi: [10.3847/1538-3881/ab4fee](https://doi.org/10.3847/1538-3881/ab4fee)
- Astropy Collaboration, Robitaille, T. P., Tollerud, E. J., et al. 2013, A&A, 558, A33, doi: [10.1051/0004-6361/201322068](https://doi.org/10.1051/0004-6361/201322068)
- Astropy Collaboration, Price-Whelan, A. M., Sipőcz, B. M., et al. 2018, AJ, 156, 123, doi: [10.3847/1538-3881/aabc4f](https://doi.org/10.3847/1538-3881/aabc4f)

- Bailer-Jones, C. A. L., Rybizki, J., Fouesneau, M., Demleitner, M., & Andrae, R. 2021, *AJ*, 161, 147, doi: [10.3847/1538-3881/abd806](https://doi.org/10.3847/1538-3881/abd806)
- Balona, L. A., Medupe, T., Abedigamba, O. P., et al. 2013, *MNRAS*, 430, 3472, doi: [10.1093/mnras/stt148](https://doi.org/10.1093/mnras/stt148)
- Barentsen, G., Hedges, C., Saunders, N., et al. 2018, arXiv e-prints, arXiv:1810.12554, <https://arxiv.org/abs/1810.12554>
- Batalha, N. M., Borucki, W. J., Koch, D. G., et al. 2010, *ApJL*, 713, L109, doi: [10.1088/2041-8205/713/2/L109](https://doi.org/10.1088/2041-8205/713/2/L109)
- Belokurov, V., Penoyre, Z., Oh, S., et al. 2020, *Monthly Notices of the Royal Astronomical Society*, 496, 1922, doi: [10.1093/mnras/staa1522](https://doi.org/10.1093/mnras/staa1522)
- Borucki, W. J., Koch, D., Basri, G., et al. 2010, *Science*, 327, 977, doi: [10.1126/science.1185402](https://doi.org/10.1126/science.1185402)
- Brewer, L., Sandquist, E. L., Mathieu, R. D., et al. 2013, in *American Astronomical Society Meeting Abstracts*, Vol. 221, American Astronomical Society Meeting Abstracts #221, 250.36
- Brown, T. M., Latham, D. W., Everett, M. E., & Esquerdo, G. A. 2011, *AJ*, 142, 112, doi: [10.1088/0004-6256/142/4/112](https://doi.org/10.1088/0004-6256/142/4/112)
- Bryson, S. T., Tenenbaum, P., Jenkins, J. M., et al. 2010, *ApJL*, 713, L97, doi: [10.1088/2041-8205/713/2/L97](https://doi.org/10.1088/2041-8205/713/2/L97)
- Choi, J., Dotter, A., Conroy, C., et al. 2016, *ApJ*, 823, 102, doi: [10.3847/0004-637X/823/2/102](https://doi.org/10.3847/0004-637X/823/2/102)
- Cody, A. M., Barentsen, G., Hedges, C., Gully-Santiago, M., & Cardoso, J. V. d. M. 2018, *Research Notes of the American Astronomical Society*, 2, 25, doi: [10.3847/2515-5172/aaac30](https://doi.org/10.3847/2515-5172/aaac30)
- Corsaro, E., Stello, D., Huber, D., et al. 2012, *ApJ*, 757, 190, doi: [10.1088/0004-637X/757/2/190](https://doi.org/10.1088/0004-637X/757/2/190)
- Cutri, R. M., & et al. 2012, *VizieR Online Data Catalog*, II/311
- Cutri, R. M., Skrutskie, M. F., van Dyk, S., et al. 2003, *VizieR Online Data Catalog*, II/246
- Dotter, A. 2016, *ApJS*, 222, 8, doi: [10.3847/0067-0049/222/1/8](https://doi.org/10.3847/0067-0049/222/1/8)
- Eastman, J., Gaudi, B. S., & Agol, E. 2013, *PASP*, 125, 83, doi: [10.1086/669497](https://doi.org/10.1086/669497)
- Eastman, J. D., Rodriguez, J. E., Agol, E., et al. 2019, arXiv e-prints, arXiv:1907.09480, <https://arxiv.org/abs/1907.09480>
- Espinoza, N., Kossakowski, D., & Brahm, R. 2019, *MNRAS*, 490, 2262, doi: [10.1093/mnras/stz2688](https://doi.org/10.1093/mnras/stz2688)
- Fabricius, C., Luri, X., Arenou, F., et al. 2021, *A&A*, 649, A5, doi: [10.1051/0004-6361/202039834](https://doi.org/10.1051/0004-6361/202039834)
- Foreman-Mackey, D., Savel, A., Luger, R., et al. 2021, *exoplanet-dev/exoplanet* v0.4.5, doi: [10.5281/zenodo.1998447](https://doi.org/10.5281/zenodo.1998447)
- Gaia Collaboration, Brown, A. G. A., Vallenari, A., et al. 2018, *A&A*, 616, A1, doi: [10.1051/0004-6361/201833051](https://doi.org/10.1051/0004-6361/201833051)
- . 2021, *A&A*, 649, A1, doi: [10.1051/0004-6361/202039657](https://doi.org/10.1051/0004-6361/202039657)
- Garnavich, P. M., Tucker, B. E., Rest, A., et al. 2016, *ApJ*, 820, 23, doi: [10.3847/0004-637X/820/1/23](https://doi.org/10.3847/0004-637X/820/1/23)
- Harris, C. R., Millman, K. J., van der Walt, S. J., et al. 2020, *Nature*, 585, 357, doi: [10.1038/s41586-020-2649-2](https://doi.org/10.1038/s41586-020-2649-2)
- Hedges, C., Luger, R., Martínez-Palomera, J., Dotson, J., & Barentsen, G. 2021a, *AJ*, 162, 107, doi: [10.3847/1538-3881/ac0825](https://doi.org/10.3847/1538-3881/ac0825)
- Hedges, C., & Martínez-Palomera, J. 2021, *SSDataLab/psfmachine: Initial Release with Paper*, v1.0.0, Zenodo, doi: [10.5281/zenodo.4784073](https://doi.org/10.5281/zenodo.4784073)
- Hedges, C., Saunders, N., & Martínez-Palomera, J. 2021b, *Research Notes of the American Astronomical Society*, 5, 260, doi: [10.3847/2515-5172/ac3765](https://doi.org/10.3847/2515-5172/ac3765)
- Jenkins, J. M., Caldwell, D. A., Chandrasekaran, H., et al. 2010, *The Astrophysical Journal*, 713, L87, doi: [10.1088/2041-8205/713/2/L87](https://doi.org/10.1088/2041-8205/713/2/L87)
- Jordi, C., Gebran, M., Carrasco, J. M., et al. 2010, *A&A*, 523, A48, doi: [10.1051/0004-6361/201015441](https://doi.org/10.1051/0004-6361/201015441)
- Kinemuchi, K., Barclay, T., Fanelli, M., et al. 2012, *PASP*, 124, 963, doi: [10.1086/667603](https://doi.org/10.1086/667603)
- Kipping, D. M. 2013, *MNRAS*, 435, 2152, doi: [10.1093/mnras/stt1435](https://doi.org/10.1093/mnras/stt1435)
- Kirk, B., Conroy, K., Prša, A., et al. 2016, *AJ*, 151, 68, doi: [10.3847/0004-6256/151/3/68](https://doi.org/10.3847/0004-6256/151/3/68)
- Kovács, G., Zucker, S., & Mazeh, T. 2002, *A&A*, 391, 369, doi: [10.1051/0004-6361:20020802](https://doi.org/10.1051/0004-6361:20020802)
- Kumar, R., Carroll, C., Hartikainen, A., & Martin, O. 2019, *Journal of Open Source Software*, 4, 1143, doi: [10.21105/joss.01143](https://doi.org/10.21105/joss.01143)
- Li, W., Wang, X., Vinkó, J., et al. 2019, *ApJ*, 870, 12, doi: [10.3847/1538-4357/aaec74](https://doi.org/10.3847/1538-4357/aaec74)
- Lightkurve Collaboration, Cardoso, J. V. d. M., Hedges, C., et al. 2018, *Lightkurve: Kepler and TESS time series analysis in Python*, *Astrophysics Source Code Library*, <http://ascl.net/1812.013>
- Lindgren, L., Hernández, J., Bombrun, A., et al. 2018, *A&A*, 616, A2, doi: [10.1051/0004-6361/201832727](https://doi.org/10.1051/0004-6361/201832727)
- Luger, R., Agol, E., Foreman-Mackey, D., et al. 2019, *AJ*, 157, 64, doi: [10.3847/1538-3881/aae8e5](https://doi.org/10.3847/1538-3881/aae8e5)
- Martínez-Palomera, J. 2021, *jorgemarpa/kepler-apertures: Kepler-apertures first release, v0.1.0*, Zenodo, doi: [10.5281/zenodo.5062871](https://doi.org/10.5281/zenodo.5062871)
- McClure, R. L., Soares, M., Mathieu, R., & Moore, C. 2021, in *American Astronomical Society Meeting Abstracts*, Vol. 53, American Astronomical Society Meeting Abstracts, 140.06

- Montet, B. T., Tovar, G., & Foreman-Mackey, D. 2017, *The Astrophysical Journal*, 851, 116, doi: [10.3847/1538-4357/aa9e00](https://doi.org/10.3847/1538-4357/aa9e00)
- Olling, R. P., Moshotzky, R., Shaya, E. J., et al. 2015, *Nature*, 521, 332, doi: [10.1038/nature14455](https://doi.org/10.1038/nature14455)
- Paxton, B., Bildsten, L., Dotter, A., et al. 2011, *ApJS*, 192, 3, doi: [10.1088/0067-0049/192/1/3](https://doi.org/10.1088/0067-0049/192/1/3)
- Paxton, B., Cantiello, M., Arras, P., et al. 2013, *ApJS*, 208, 4, doi: [10.1088/0067-0049/208/1/4](https://doi.org/10.1088/0067-0049/208/1/4)
- Paxton, B., Marchant, P., Schwab, J., et al. 2015, *ApJS*, 220, 15, doi: [10.1088/0067-0049/220/1/15](https://doi.org/10.1088/0067-0049/220/1/15)
- Salvatier, J., Wiecki, T. V., & Fonnesbeck, C. 2016, *PeerJ Computer Science*, 2, e55, doi: [10.7717/peerj-cs.55](https://doi.org/10.7717/peerj-cs.55)
- Sandford, E., & Kipping, D. 2017, *The Astronomical Journal*, 154, 228, doi: [10.3847/1538-3881/aa94bf](https://doi.org/10.3847/1538-3881/aa94bf)
- Schlafly, E. F., & Finkbeiner, D. P. 2011, *ApJ*, 737, 103, doi: [10.1088/0004-637X/737/2/103](https://doi.org/10.1088/0004-637X/737/2/103)
- Schlegel, D. J., Finkbeiner, D. P., & Davis, M. 1998, *ApJ*, 500, 525, doi: [10.1086/305772](https://doi.org/10.1086/305772)
- Smith, J. C., Stumpe, M. C., Van Cleve, J. E., et al. 2012, *PASP*, 124, 1000, doi: [10.1086/667697](https://doi.org/10.1086/667697)
- Stello, D., Basu, S., Bruntt, H., et al. 2010, *ApJL*, 713, L182, doi: [10.1088/2041-8205/713/2/L182](https://doi.org/10.1088/2041-8205/713/2/L182)
- Stello, D., Huber, D., Kallinger, T., et al. 2011, *ApJL*, 737, L10, doi: [10.1088/2041-8205/737/1/L10](https://doi.org/10.1088/2041-8205/737/1/L10)
- The Theano Development Team, Al-Rfou, R., Alain, G., et al. 2016, arXiv e-prints, arXiv:1605.02688. <https://arxiv.org/abs/1605.02688>
- Thompson, S. E., Fraquelli, D., Van Cleve, J. E., & Caldwell, D. A. 2016, *Kepler Archive Manual*, Kepler Science Document KDMC-10008-006
- Thompson, S. E., Coughlin, J. L., Hoffman, K., et al. 2018, *The Astrophysical Journal Supplement Series*, 235, 38, doi: [10.3847/1538-4365/aab4f9](https://doi.org/10.3847/1538-4365/aab4f9)
- Van Cleve, J. E., & Caldwell, D. A. 2016, *Kepler Instrument Handbook*, Kepler Science Document KSCI-19033-002
- Van Cleve, J. E., Christiansen, J. L., Jenkins, J. M., et al. 2016, *Kepler Data Characteristics Handbook*, Kepler Science Document KSCI-19040-005
- Vanderburg, A., & Johnson, J. A. 2014, *PASP*, 126, 948, doi: [10.1086/678764](https://doi.org/10.1086/678764)
- Virtanen, P., Gommers, R., Oliphant, T. E., et al. 2020, *Nature Methods*, 17, 261, doi: [10.1038/s41592-019-0686-2](https://doi.org/10.1038/s41592-019-0686-2)
- Wu, H., Twicken, J. D., Tenenbaum, P., et al. 2010, in *Society of Photo-Optical Instrumentation Engineers (SPIE) Conference Series*, Vol. 7740, *Software and Cyberinfrastructure for Astronomy*, ed. N. M. Radziwill & A. Bridger, 774019, doi: [10.1117/12.856630](https://doi.org/10.1117/12.856630)